



Cite this: *Digital Discovery*, 2024, **3**, 287

Received 8th August 2023
Accepted 7th December 2023

DOI: 10.1039/d3dd00149k
rsc.li/digitaldiscovery

1 Introduction

Predicting protein–ligand interaction (PLI) plays a critical role in the early stages of drug discovery.^{1–3} It can be mainly utilized for two purposes: virtual screening to efficiently identify hit candidates from a large chemical space for a target protein and a process designed to refine these discovered molecules to increase their affinities. The virtual screening emphasizes cost-effectiveness due to the extensive calculation required,^{4,5} while the accuracy is more important for the binding affinity improvement process due to the need for the precise evaluation of a relatively smaller number of molecules.^{6,7} In this light, both fast and accurate PLI prediction is necessary to meet these requirements. An ideal PLI prediction model should be computationally efficient and accurate in predicting binding affinity and thus be able to correlate the prediction with experimental binding affinities or correctly distinguish active and inactive molecules.^{8,9}

Inspired by the earlier success of machine learning-based approaches for PLI prediction,^{10–12} deep learning-based models have attracted great attention recently.^{13–16} Deep learning allowed for retaining fast computation speed while

demonstrating high performance in predicting the binding affinities of protein–ligand crystal structures.¹⁷ Despite their potential, most deep learning-based PLI prediction models are insufficient to be applied to various tasks at once.^{18–21} Instead, they are task-specific, focusing only on scoring,^{16,22,23} pose optimization,^{24–26} or screening.²⁷ Specifically, the scoring task is to predict the binding affinities of protein–ligand complexes, and the screening task is to classify different compounds into true binders and non-binders. Contrary to the common expectation that a model with high accuracy in binding affinity scoring will also have high accuracy in virtual screening, the performance of these two tasks is often at odds because deep learning models tend to learn exclusive (rather than generalizable) features to perform best at each task. For example, models for predicting binding affinities trained only on crystal structures performed well at scoring crystal or near-native structures but struggled with tasks such as identifying specific binders to a target protein among diverse molecules or evaluating computer-generated structures as required in virtual screening.²⁸ Meanwhile, models that employ a Δ -learning strategy with computer-generated data^{27,29} or target the binding pose optimization^{24,25} have shown improved performance in virtual screening but failed to rank the relative binding affinities of different protein–ligand complexes adequately. These challenges underscore the difficulty in designing a versatile PLI prediction model that can effectively handle diverse tasks.

Designing a versatile deep learning-based PLI prediction model performing well on both scoring and screening is challenged by the low generalizability of the model, which is mainly

^aDepartment of Chemistry, KAIST, 291 Daehak-ro, Yuseong-gu, Daejeon 34141, Republic of Korea. E-mail: wooyoun@kaist.ac.kr

^bHITS Incorporation, 124 Teheran-ro, Gangnam-gu, Seoul 06234, Republic of Korea

^{AI} Institute, KAIST, 291 Daehak-ro, Yuseong-gu, Daejeon 34141, Republic of Korea

† Electronic supplementary information (ESI) available. See DOI: <https://doi.org/10.1039/d3dd00149k>





due to the lack of well-curated structure-affinity data.^{30–32} This challenge persists despite the gradually increasing availability of binding structure data from experiments.³³ To overcome this hurdle, one can impose a generalizable inductive bias throughout various tasks into the model. In the previous study, we have shown that incorporating the physics of non-covalent molecular interaction as an inductive bias improves the generalization ability of a deep learning-based PLI prediction model.³⁴ In addition, data augmentation strategies can mitigate the problem of the lack of experimental structure-affinity data. Previous approaches adopted data augmentation strategies by training the model with docking-generated structures to predict the binding affinities of non-binding structures to be less than that of experimental structures.^{35,36} These strategies are based on the physical intuition that highly divergent structures of cognate ligands or structures with non-cognate ligands for a given target would have weaker binding affinities than a crystal structure of a true binder. However, models trained only with such augmented data have exhibited a relative decrease in scoring performance, diminishing their utility for this particular task.^{34,37}

Recently, GenScore³⁸ reported state-of-the-art performance on various tasks, including scoring and screening.‡ It is noteworthy that GenScore used neither physics-based inductive bias nor data augmentation and simply focused on learning the distance likelihood of binding structures instead of predicting their binding affinities. Direct prediction of binding affinities has the great advantage that the predicted values can be directly compared to the experimental results, allowing for an intuitive explanation and directions for further improvement, whereas distance likelihood-based results only allow for relative comparisons between predicted values.

Here, we propose a versatile deep learning-based PLI prediction model by improving its generalization ability with physics-based inductive bias and data augmentation strategy. Along with the previous data augmentation strategies, we generated near-native structures that are energetically and geometrically similar to crystal structures to consider their limited experimental resolution and intrinsic dynamic nature *in vivo*. The model was then trained to predict the binding affinities of these structures to be the same as the corresponding experimental values, effectively recognizing that these structures lie on the same local minima as crystal structures. As a result, PIGNet2, which is based on a physics-informed graph neural network modified from our previous work,³⁴ showed significantly enhanced scoring and screening performance.

To demonstrate the potential applicability of PIGNet2 in scoring and screening tasks, we evaluated it against various benchmarks. We note that there are diverse machine learning and deep learning models for each benchmark with different purposes.^{39–43} Instead of comprehensively reviewing such existing models, our evaluation focuses on comparing PIGNet2 with the

best deep learning-based PLI prediction models for each benchmark alongside traditional docking programs in the perspective of the model's versatility. We used the CASF-2016 benchmark⁴⁴ to compare the overall performance on scoring, docking, and screening. Following that, we also used DUD-E⁴⁵ and DEKOIS2.0 (ref. 46) as widely adopted virtual screening benchmarks to evaluate the screening performance in more detail. To further assess the scoring performance, we adopted two separate derivative benchmarks provided by Wang *et al.*⁴⁷ and the Merck FEP benchmark,⁴⁸ which will be called the derivative benchmark 2015 and 2020, respectively. Both are the structure-affinity datasets of derivative compounds with various target proteins and are specifically designed for assessing the scoring performance of PLI prediction models between structurally similar molecules. Overall, PIGNet2 outperformed task-specific models in all benchmarks, achieving results on par with the state-of-the-art performance of GenScore while leaving room for further improvement thanks to its use of intuitively explainable physics. Thus, our approach provides an alternative solution to develop a versatile deep learning model that can be used for hit identification and lead optimization in drug discovery.

2 Methods

2.1 PDBbind dataset

The PDBbind dataset,⁴⁹ which comprises protein–ligand binding complex data curated from the Protein Data Bank (PDB),⁵⁰ is divided into general, refined, and core sets based on the strictness of the curation. The core set is subjected to the most rigorous curation criteria, thus including representative entities with respect to a corresponding target protein. A growing trend among recent PLI prediction models is to exploit the general set in order to leverage a larger pool of crystal structures for training.^{35,36} This approach was inspired by a previous work demonstrating that using the larger general set can improve the performance of PLI prediction models when compared to the refined set.⁵¹

In our study, however, we employed the refined set to carry out data augmentation for all the proteins and ligands with limited computational resources. This may indicate that our model still has room for improvement by expanding the number of crystal structure data with the general set. Of the 5312 complexes present in the refined set, we omitted the core set included in the CASF-2016 benchmark⁴⁴ and redundant complexes. As a result, we ended up with a training set of 5046 complexes and a test set of 266 complexes. To alleviate an undesired overfitting issue possibly coming from the limited number of crystal structures, we employed data augmentation strategies as described in the next section.

2.2 Data augmentation strategies

In this section, we present our novel positive data augmentation (PDA) strategy in conjunction with various negative data augmentation (NDA) strategies: re-docking, random-docking, and cross-docking data augmentation.

‡ Shortly before our submission, we became aware of the recently published GenScore. To ensure that our paper is comprehensive and up-to-date, we included a comparative analysis of our model with the results presented in the GenScore study.

2.2.1 Positive data augmentation. Recent deep learning-based PLI prediction models commonly utilize crystal structures and docked structures from NDA as input, where the unnatural NDA-generated structures get substantially more abundant than crystal structures. We hypothesize that this data imbalance potentially impedes the discrimination between near-native and unnatural (or unstable) structures, thereby degrading the performance of binding affinity prediction for crystal or near-native structures. Since each crystal structure is a single snapshot of conformations around local minima of a potential energy surface, near-native structures around the crystal structure can also be regarded as true binders. Thus, a large number of near-native structures can be sampled by slightly altering the ligand pose from the crystal structure within a certain experimental resolution, which helps avoid the imbalance problem. Moreover, the consideration of the near-native structures may implicitly integrate the conformational ensemble effect into the PLI prediction model, leading to more reliable prediction. In this light, we introduced a novel data augmentation strategy, PDA, designed to generate energetically and geometrically near-native conformations for any given complex structure. This is one of the key distinctions of PIGNet2 from the original one.

For PDA, we first generated 1000 conformations of each ligand using the ETKDG conformer generation method.⁵² We optimized those structures using the universal force field (UFF)⁵³ and Merck molecular force field (MMFF).⁵⁴ This can yield a maximum of 3000 data points for each complex. Next, the resulting structures were aligned to the ligand's pose in the crystal. Finally, the structures are minimized using the Smina docking software,⁵⁵ a forked version of AutoDock Vina,⁵⁶ to avoid clashes. We then selected structures that satisfy two criteria: (1) a ligand root mean square deviation (RMSD) less than 2 Å compared to the crystal structure and (2) a mean absolute error less than 1 kcal mol⁻¹ between the Smina scores of the crystal structure and the generated structures. The latter criterion aims to select structures energetically similar to the near-native structure, in addition to the former, the geometric criterion that is more generally used. While the scoring function of Smina only approximates the PLI potential energy surface (PES), it is rational to regard structures with similar scores in a confined range as energetically near-native on the actual PES considering the continuity of energy. Finally, to remove highly similar structures that can be considered duplicates, we additionally pruned the generated structures so that the RMSD between every pair of the generated structures is greater than 0.25 Å. Along with the above, structures generated by re-docking crystal structures using Smina were also used, where the RMSD between every pair of generated structures for each complex was maintained below 2 Å.

2.2.2 Negative data augmentation. One of the goals of negative data (decoy) generation is to reduce false negatives in prediction. To achieve this, the conventional strategy for the decoy generation sampled structurally different molecules in 2D from known positives for a given target as negatives.^{45,57} Instead, we attempted to consider more 3D structural

information during the decoy generation. For structure-based approaches like PIGNet2, generating the decoys at the pose level is as important as at the molecular species level, because the same ligand can be either active or inactive depending on its binding pose. This can promote the model to learn 3D interaction features rather than simply memorizing ligand features.

The NDA strategies mostly follow the methods outlined in our previous work.³⁴ However, we adopted additional guidelines here for a more rigorous generation of non-binding structures. First, the re-docking data augmentation generates structures by docking ligands into a cognate target and then extracting unstable structures. Based on the fact that crystal structures are stable binding poses, one can infer that ligand structures that deviate significantly from the crystal structure will be highly unstable. Thus, we used docking-generated structures with the ligand RMSD greater than 4 Å compared to the corresponding crystal structure. Second, cross-docking data augmentation uses the idea that a non-cognate protein-ligand pair is less likely to form a bound complex. To implement this, we grouped proteins based on a protein sequence similarity of 0.4 using the cd-hit software.^{58,59} Then, pairs of different protein clusters were sampled, and for each pair of clusters, proteins from one cluster were docked with ligands from the other cluster to generate structures of non-cognate protein-ligand pairs. The additional filtration criteria based on the ligand RMSD and protein sequence similarity are expected to provide stricter deviation of negatively augmented data from near-native data. Lastly, the random-docking data augmentation strategy assumes that an arbitrarily chosen molecule is unlikely to be a true binder to a given protein by chance. This was intended to incorporate a structural diversity of decoys because the re-docking and cross-docking data augmentation strategies only treat a limited number of molecules. We generated the corresponding structures by docking a random molecule from the IBS molecule dataset⁶⁰ to each protein. However, as we did not add explicit rules to filter false negatives in the random-docking augmentation, we expect that a better generation strategy of decoys such as the conventional methods^{45,57} will improve the screening performance of the model.

For all the negative data augmentation strategies, we used Smina for docking and structure minimization and the DockRMSD⁶¹ software for calculating the ligand RMSD.

2.3 Data preprocessing

We preprocessed crystal and computer-generated structures for the PLI prediction model. Proper protonation of each molecule is crucial in this step to enhance the accurate representation of

Table 1 Number of data points generated from each data augmentation strategy

Data augmentation strategy	Training set	Test set
PDA	375 184	21 377
NDA (re-docking)	254 163	12 109
NDA (cross-docking)	503 073	26 470
NDA (random-docking)	957 775	50 496



specific physical interactions such as hydrogen bonding. To this end, we protonated all the protein structures with the Reduce software.⁶² For the ligands, we protonated them at pH 7.4 using Dimorphite-DL.⁶³ Water and hydrogens were removed from the complexes. As the final step, only the protein residues containing heavy atoms within 5 Å or less from the ligand were extracted and used as the protein pocket. We used RDKit,⁶⁴ Open Babel,⁶⁵ and PyMOL⁶⁶ throughout the overall data pre-processing. A detailed breakdown of the training and test sets, derived through each data augmentation, is presented in Table 1.

2.4 Model architecture

PIGNet2 shares the model architecture and physics terms from our previous work³⁴ except for the initial atom features and the van der Waals interaction term. Refer to ESI† for the modified initial atom features of PIGNet2.

The overall scheme of PIGNet2 is depicted in Fig. 1. PIGNet2 works as follows. Preprocessed pocket and ligand structures with input features are first passed through a feedforward network and then through a gated graph attention network, which updates atom features based on intramolecular edges. The resulting pocket and ligand features are then passed through an interaction network, which allows the embedding of additional information from the interaction counterpart *via* the intermolecular edges. Finally, the pocket and ligand features are concatenated to calculate the intermolecular atom–atom pairwise interaction terms. We refer to the previous work³⁴ for more details of the model architecture.

The total binding affinity E^{pred} predicted by the model is the sum of all intermolecular atom pairwise interactions consisting of four terms: E^{vdW} , $E^{\text{H-bond}}$, E^{Metal} , and $E^{\text{Hydrophobic}}$. Each of them represents intermolecular van der Waals (vdW), hydrogen bond, metal–ligand, and hydrophobic interactions, respectively. In order to incorporate the effect of entropy as regularization, the total energy is divided by T^{rot} , a term proportionate to the number of rotatable bonds of the ligand. The equation of the total energy is as follows:

$$E^{\text{pred}} = \frac{E^{\text{vdW}} + E^{\text{H-bond}} + E^{\text{Metal}} + E^{\text{Hydrophobic}}}{T^{\text{rot}}}. \quad (1)$$

One feature of our current model that differs from the previous is the introduction of the Morse potential instead of the Lennard-Jones potential for E^{vdW} . The ability of PIGNet2 to score the binding affinity of crystal structures or to clearly distinguish between active and decoy molecules is highly dependent on the modeling of the vdW potential well. For example, an overly broad potential well could result in the prediction of a degree of interaction even for atom pairs that are too far apart to contribute significantly to the interaction, resulting in predicting inherently unstable structures to be stable. On the other hand, an excessively narrow potential well could lead to the prediction of repulsive vdW interactions for atom pairs that are appropriately close, resulting in predicting unstable energies for them. The correct form of the potential well is, therefore, critical for accurate prediction. Thus, directly adjusting the potential well offers significant advantages in the design and evaluation of deep learning-based

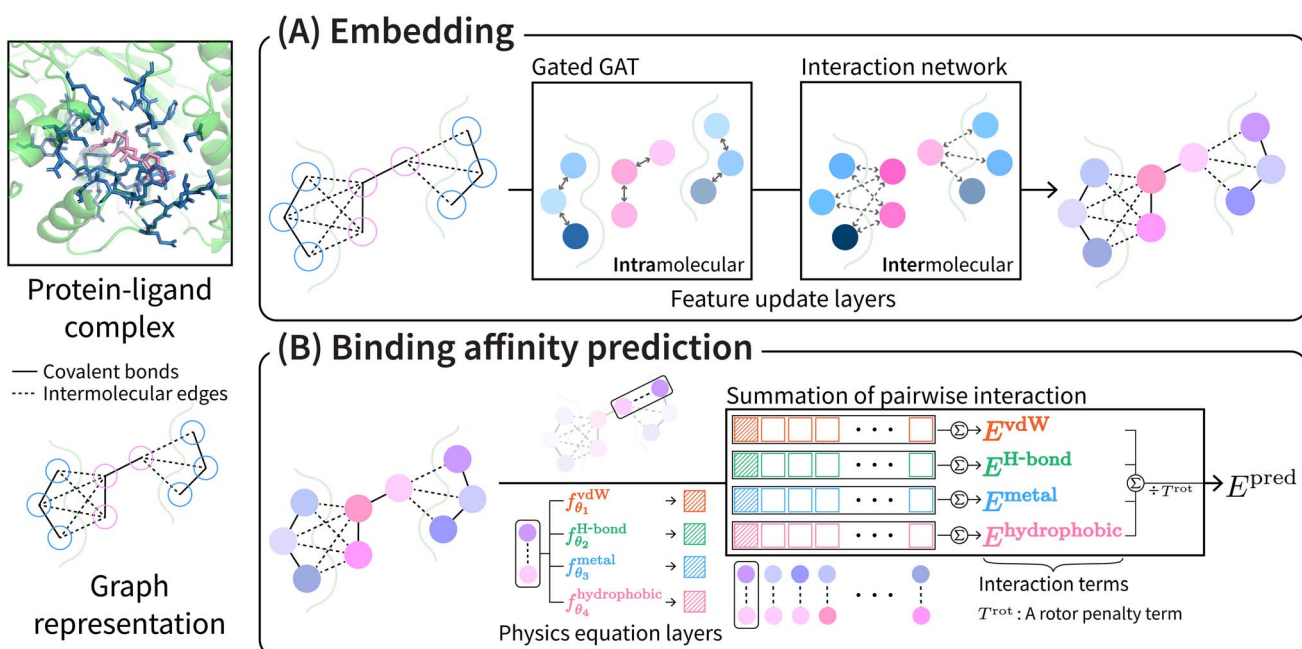


Fig. 1 The overall scheme of PIGNet2. (A) A preprocessed protein–ligand complex is sequentially fed into a gated graph attention network (GatedGAT) and an interaction network. The networks update atom features based on intra- and intermolecular edges upon each convolution, respectively. (B) Four parameterized physics terms compute intermolecular atom–atom pairwise interaction from the updated data. The total energy E^{pred} is computed by summing all interactions for all atomic pairs, divided by a rotor penalty term T^{rot} . Note that the architecture of PIGNet2 shares with its previous version except for the initial atom features and the van der Waals interaction (see methods for more details).



physics-informed PLI prediction models. However, the Lennard-Jones potential possesses insufficient flexibility to freely adjust the width of the potential well, which was our reason for introducing the derivative loss in the previous work.³⁴ As a more direct and precise alternative, we chose to use the Morse potential, which allows for explicitly controlling the potential well. For an intermolecular pair of *i*th and *j*th atoms, the van der Waals interaction e_{ij}^{vdW} in terms of the Morse potential is computed as follows:

$$e_{ij}^{vdW} = w_{ij}((1 - e^{-a_{ij}(d_{ij}-r_{ij})^2})^2 - 1), \quad (2)$$

where d_{ij} denotes the interatomic distance between the atom pair and r_{ij} is the sum of vdW radii of the atom pair. The total vdW interaction term, E^{vdW} , is computed by summing e_{ij}^{vdW} over all atom pairs. Note that we used r_{ij} as the pairwise sum of vdW radii instead of the corrected pairwise sum of vdW radii used in the previous model,³⁴ and it is used not only for the Morse potential but also for all the other physics terms. The coefficient a_{ij} modulates the width of the potential well, while w_{ij} affects the depth of the potential well. For the case where d_{ij} is greater than r_{ij} , the coefficient a_{ij} is predicted by the neural network, while for the opposite case, it is set as a hyperparameter, with a value of 2.1 chosen for PIGNet2.

2.5 Training setup

2.5.1 Loss function. PIGNet2 employs various loss functions to optimize the model through the learning objectives of each data augmentation strategy. Specifically, both PDA and crystal structures are used in training in conjunction with the mean squared error loss. This approach induces the model to precisely predict the experimental binding affinity for near-native structures as well as crystal structures to inform the model that the structures from PDA and crystal structures belong to the same local minima in PES. In contrast, for data exhibiting significant structural deviations from the crystal structure, which is derived from the re-docking process of NDA, we employed a hinge loss to predict a lower binding affinity than that of the crystal structure. Lastly, we applied a hinge loss for cross-docking and random-docking data augmentation in another way. This guides the model to predict binding affinity for these structures higher than a criterion of -6.8 kcal mol⁻¹, consistent with the assumption that these structures are unlikely to have a binding interaction. Altogether, the total loss function is a weighted sum of all the losses above. A more detailed description of the loss function is shown in the ESI.†

2.5.2 Training procedure. During the training with PDA, we merged the PDA and crystal structures into a single dataset. Meanwhile, during the training with NDA, we set the number of data for each dataset that the model learns per epoch to be equal. Throughout the training, we used a batch size of 64, a learning rate of 0.0004, and a dropout ratio of 0.1. We used a single RTX A4000 GPU for all training and inference. Finally, all our results are an ensemble of predictions from four models, each initialized with a different random seed.

3 Results and discussion

3.1 Performance on CASF-2016 benchmark

3.1.1 CASF-2016 benchmark. To demonstrate the versatility of PIGNet2 for broad applications, we employed the well-established CASF-2016 benchmark.⁴⁴

The CASF-2016 benchmark was carefully curated from 285 protein-ligand complexes in the PDBbind core set. This benchmark provides a comprehensive set of four metrics: scoring power, ranking power, docking power, and screening power. Each metric has a unique purpose in assessing PLI prediction models.

The metrics fall into two main categories. The first category evaluates the ability of the model to predict binding affinity for crystal structures. The second category evaluates the ability of the model to distinguish true-binding structures from various computer-generated structures. Scoring power and ranking power fall into the first category, and docking power and screening power fall into the second category. The four metrics comprehensively evaluate models' performance in different aspects of PLI prediction.

Specifically, the scoring power evaluates the ability of the model to predict the binding affinity of protein-ligand crystal structures and is assessed using the Pearson correlation coefficient R . The ranking power measures the ability of the model to rank the binding affinities of protein-ligand complexes grouped by protein similarity. It is evaluated using the Spearman rank correlation coefficient ρ . The docking power assesses the ability of the model to identify near-native structures from computer-generated decoy structures. The metric is evaluated based on a top N success rate, SR_N , where a case is considered successful if at least one of the top N predicted structures for each complex has a ligand root mean square deviation (RMSD) of less than 2 Å when compared to the crystal structure. Finally, the screening power evaluates the ability of the model to identify cognate protein-ligand complexes that can form a binding interaction among the vast amount of non-cognate protein-ligand complexes in cross-docking scenarios. The screening power is assessed with the top $\alpha\%$ enrichment factor, $EF_{\alpha\%}$, which is a measure of the ratio of active molecules included in the top $\alpha\%$ model predictions to the total number of active molecules, defined as follows:

$$EF_{\alpha\%} = \frac{NTB_{\alpha}}{NTB_{\text{total}} \times \alpha}, \quad (3)$$

where NTB_{α} is the number of active molecules in top $\alpha\%$ and NTB_{total} is the total number of active molecules in the overall dataset. Along with $EF_{\alpha\%}$, we also report the top $\alpha\%$ success rate, $SR_{\alpha\%}$, which measures the success rate of finding the best binder among the top $\alpha\%$ top-ranked structures for all targets.

3.1.2 Baseline models. We selected several task-specific deep learning-based PLI prediction models as baselines for comparative studies. These models differ in their prediction targets during training and inference, tailored to excel in their respective objective tasks. Thus, the models are categorized based on their prediction targets: distance likelihood, Δ binding affinity, and exact binding affinity, to differentiate the



results from previous approaches better. Our model, PIGNet2, falls into the category that directly predicts exact binding affinity.

DeepDock²⁴ primarily aims to optimize protein–ligand structures. Instead of predicting binding affinities, DeepDock predicts the distance likelihood of given structures by utilizing a mixture density network⁶⁷ to model the statistical potential of protein–ligand structures. GenScore,³⁸ a model built on the same formulation as DeepDock, is trained with an additional loss term to learn the correlation between the binding affinities of different complexes. Since the authors provide ten models with different adjustable parameters and each showed different performances in various tasks, here we report the results of GT_ft_0.5 and GatedGCN_ft_1.0, which respectively showed the best performances in screening and scoring.

Unlike previous methods, OnionNet-SFCT²⁷ and Δ -AEScore²⁹ estimate the final energy by a linear combination of correction terms to the Autodock Vina⁵⁶ scores. These methods incorporate various computer-generated structures in their training process to enhance performance in virtual screening tasks.

Finally, baseline models that directly predict exact binding affinity include AK-score,¹⁶ Sfenn,²³ OnionNet-2,²² and AEScore.²⁹ AK-score and Sfenn use 3D convolutional neural networks (CNN), while OnionNet-2 uses a 2D feature map with a 2D CNN. AEScore predicts binding affinities using a feedforward neural network based on an atomic environment vector representation. By including these different models in our comparison, we can thoroughly evaluate the relative performance and robustness of PIGNet2.

3.1.3 Performance of PIGNet2. The performance of PIGNet2 is shown in Table 2 along with all known results from the baseline models. DeepDock, a model that predicts distance likelihood, showed excellent performance in distinguishing crystal structures from computer-generated structures, which is evident with their high docking and screening powers. However, its ability to predict or compare the binding affinity of crystal structures is limited. This is because their distance

likelihood computation can only infer the relative stability of conformations of a single protein–ligand complex. This makes it difficult to compare different protein–ligand complexes of stable structures, mirroring the limitations of traditional knowledge-based PLI prediction models that also utilized statistical potentials. GenScore overcomes this difficulty by introducing an additional loss term that guides it to learn the correlation between experimental binding affinities and the statistical potentials based on the distance likelihood, achieving state-of-the-art performances in both scoring and screening tasks.

Models focusing on accurate regression of binding affinities generally demonstrate their strong performance in scoring and ranking. Nevertheless, their performance on virtual screening-related metrics lags behind those predicting distance likelihoods. Prime examples of such models include AEScore and OnionNet-2, and they have attempted to compensate for the poor screening performance by introducing various computer-generated structures and Δ -learning. Although the resulting OnionNet-SFCT and Δ -AEScore enhanced docking and screening power, their scoring and ranking powers were significantly reduced. This trend was particularly pronounced for OnionNet-SFCT, indicating that designing versatile deep learning-based PLI prediction models is challenging even with data augmentation and Δ -learning.

PIGNet2 aimed to perform equally well in all tasks using a physics-informed graph neural network coupled with various data augmentation strategies. Indeed, PIGNet2 demonstrated high performance for all metrics, comparable to the state-of-the-art performance of GenScore, while GenScore slightly outperformed PIGNet2 depending on its various versions. PIGNet2 outperformed the result of DeepDock in its primary objective, *i.e.*, pose optimization, as shown by the docking power. Specifically, PIGNet2 attained scoring and ranking powers comparable to those of OnionNet-2, AEScore, AK-score, and Sfenn, all of which aim to accurately score the binding affinities of crystal structures. PIGNet2 outperformed in all metrics, compared to OnionNet-SFCT and Δ -AEScore. These results

Table 2 Results on the CASF-2016 benchmark. EF_{1%}, SR_{1%}, SR₁, *R*, and ρ are top 1% enrichment factor, top 1% success rate, top 1 success rate, Pearson correlation coefficient, and Spearman rank correlation coefficient, respectively. Note that EF_{1%}, SR_{1%}, and SR₁ are averaged values through targets. The results of all baseline PLI prediction models originated from their respective literature. For PIGNet2, we report the results of 4 randomly initialized model ensembles trained with both positive data augmentation and negative data augmentation. The best performance is shown in bold, while the second-best is shown in the italics

Model	Prediction target	Screening power		Docking power		Scoring power		Ranking power	
		EF _{1%}	SR _{1%}	SR ₁	<i>R</i>	ρ			
DeepDock ²⁴	Distance likelihood	16.4	43.9%	89.1%	0.460	0.425			
GenScore (GT_ft_0.5) ³⁸	Distance likelihood	28.2	71.4%	97.6%	0.773	0.659			
GenScore (GatedGCN_ft_1.0) ³⁸	Distance likelihood	23.5	66.1%	95.4%	0.834	0.686			
OnionNet-SFCT (Vina) ²⁷	Δ binding affinity	15.5	—	93.7%	0.428	0.393			
Δ -AEScore ²⁹	Δ binding affinity	6.16	19.3%	85.6%	0.740	0.590			
OnionNet-2 (ref. 22)	Exact binding affinity	—	—	—	0.864	—			
AEScore ²⁹	Exact binding affinity	—	—	35.8%	0.830	0.64			
AK-score ¹⁶	Exact binding affinity	—	—	36.0%	0.812	0.670			
Sfenn ²³	Exact binding affinity	—	—	34.0%	0.795	—			
PIGNet2	Exact binding affinity	24.9	66.7%	93.0%	0.747	0.651			



support that PIGNet2 can serve as a versatile deep learning-based PLI prediction model.

3.2 Performance on classifying active and decoy compounds

While the CASF-2016 screening benchmark is well-designed and offers extensive structure data, it is different from real-world virtual screening scenarios. This is because of relatively fewer actives and decoys; the screening benchmark was curated by cross-docking between 57 protein clusters with a total of 285 protein-ligand complexes, so the number of active and decoy compounds is 5 and 280 at maximum, respectively. To evaluate the screening performance of PIGNet2 in a larger library, we used the Directory of Useful Decoys-Enhanced (DUD-E)⁴⁵ and Demanding Evaluation Kits for Objective *In silico* Screening (DEKOIS) 2.0.⁴⁶ These benchmarks comprise a much larger number of active and decoy compounds compared to CASF-2016, with a higher active-to-decoy ratio.

3.2.1 Virtual screening benchmark. The DUD-E benchmark is widely used for evaluating the virtual screening performance of PLI prediction models. Each of the 102 total targets has hundreds of active compounds and thousands of decoy compounds. While some studies have criticized the DUD-E benchmark for its hidden biases that hinder the generalization of PLI prediction models,^{19,68} most of these investigations are based on the results of training and inference conducted using the DUD-E benchmark. We expect that generalizability issues may not be critical in our case because PIGNet2 was not trained on the DUD-E data. We additionally adopted DEKOIS2.0, which comprises 81 different targets. Like the DUD-E benchmark, DEKOIS2.0 contains dozens of active compounds and thousands of decoys for each target. It should be noted that we did not exclude any data in the benchmarks for a direct comparison with other models, although the two benchmark sets share several target proteins with the training set.

To conduct a comparative assessment of PIGNet2 with other models, we selected the top $\alpha\%$ enrichment factor as our primary benchmark metric, consistent with the CASF-2016 screening benchmark. We also adopted area under the receiver operating characteristic curve (AUROC)⁶⁹ and Boltzmann enhanced discrimination of receiver operating characteristic curve (BEDROC)⁷⁰ along with the enrichment factor. The BEDROC has an α term to adjust the criterion of early recognition, and we set it as the same value of 80.5 used in GenScore for a direct comparison. Both AUROC and BEDROC range from 0 to 1; the higher the value, the better the model's performance in classification and assigning early ranking for active compounds, respectively. Additionally, to conduct an ablation study on data augmentation in the context of screening performance, we used the Kullback-Leibler (KL) divergence, D_{KL} .⁷¹ The KL divergence measures the deviation between the predicted binding affinity distributions, D_{active} and D_{decoy} , of actives and decoys, respectively, which is given as follows:

$$D_{KL}(D_{active} \| D_{decoy}) = - \sum_{x \in X} D_{active}(x) \log \left(\frac{D_{decoy}(x)}{D_{active}(x)} \right). \quad (4)$$

The KL divergence always has a positive value, and the higher the value, the greater the deviation between D_{active} and D_{decoy} .

3.2.2 Baseline models. We adopted three deep learning-based PLI prediction models for the comparative analysis. OnionNet-SFCT predicts correction terms for the scoring function of docking programs, as previously mentioned in section 3.1.2. We chose the model that predicts a scoring function correction term for Autodock Vina.⁵⁶ GenScore predicting the distance likelihood was one of the best PLI prediction models in the screening performance. GNINA is a 3D CNN-based model trained using various data augmentation strategies and tasks like PIGNet2. GNINA offers several models for the virtual screening. Here, we chose the dense (affinity) model, namely dense, which showed state-of-the-art results among exact binding affinity prediction models in a previous work.⁷²

3.2.3 Performance of PIGNet2. Fig. 2(A) shows the average DUD-E top 1% enrichment factor, $EF_{1\%}$, for PIGNet2 and the baseline models. For the evaluation of the screening performance of PIGNet2, we rescored the docking-generated structures of actives and decoys for a given target provided by GenScore.³⁸ The top 10 structures originally generated and scored using Glide SP underwent further minimization with Smina. PIGNet2 showed much higher performance than OnionNet-SFCT (Vina) and GNINA, which is close to the state-of-the-art results of GenScore. It is worth noting that these results could be influenced by potential biases arising from different numbers of sampled structures with different sampling algorithms for each method. For instance, the results of OnionNet-SFCT (Vina) were computed based on the best binding pose generated by Autodock Vina, whereas GNINA used nine structures generated by its own algorithm, and GenScore and PIGNet2 used 10 structures as described above.

To mitigate such possible biases, we further investigated the performance of PIGNet2 by using only the best pose generated by Smina and compared the results with those of OnionNet-SFCT (Vina). The resulting $EF_{1\%}$, 24.3, was denoted as PIGNet2* in Fig. 2(A), which was significantly dropped from the result with the top 10 structures (31.2) but is still far better than OnionNet-SFCT (Vina).

Table 3 shows the average AUROCs, BEDROC ($\alpha = 80.5$), top 0.5%, 1.0%, and 5.0% enrichment factors for the DEKOIS2.0 and DUD-E benchmark. We adopted the same structures provided from Hou *et al.*³⁸ since all values of the baseline models were taken from Hou *et al.*³⁸ For each complex, the top ten structures were generated by Glide SP⁷³ in the original dataset, but we further minimized them using Smina for PIGNet2. PIGNet2 outperformed Glide SP in every metric, validating its superior capability in the virtual screening task. Also, it achieved the best or second-best performance for most metrics compared to the previous state-of-the-art model, GenScore. In the case of DEKOIS2.0, PIGNet2 showed competitive performance to GenScore (GT_ft_0.5) for $EF_{0.5\%}$, an optimal one for screening among its various versions, while surpassing GenScore (GatedGCN_ft_1.0), an optimal model for scoring. As for AUROC, BEDROC ($\alpha = 80.5$), $EF_{1\%}$ and $EF_{5\%}$, PIGNet2 showed slightly better performance than both versions of



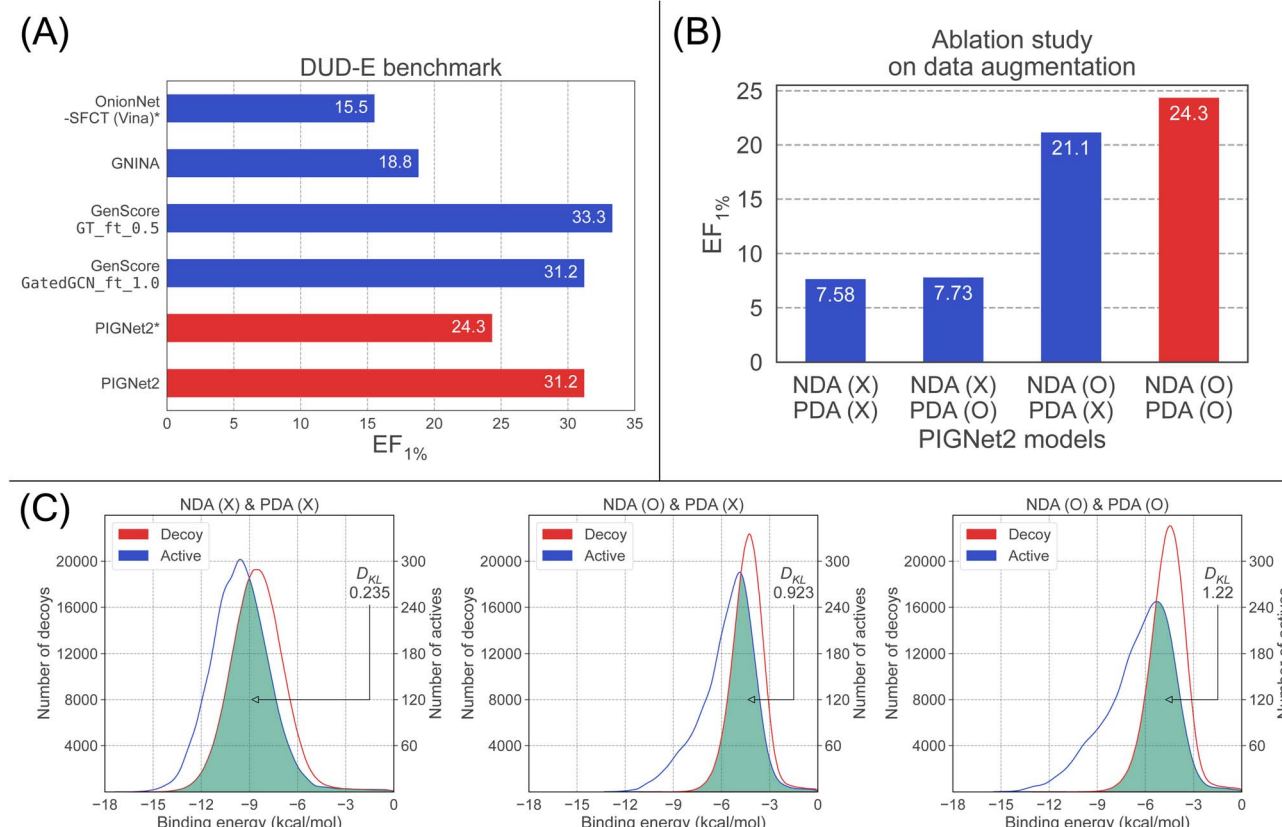


Fig. 2 Results for the DUD-E benchmark. EF_{1%} is the top 1% enrichment factor. (A) Comparison between baseline models and PIGNet2 in terms of the EF_{1%}. The models with the asterisk (*), OnionNet-SFCT (Vina) and PIGNet2, used a single conformation generated by docking, while the others used multiple conformation. (B) Ablation study about data augmentation strategies for PIGNet2 on the enrichment factor of the DUD-E benchmark. We conducted all experiments in the ablation study with the same dataset used in the result of PIGNet2* in (A), which employed only the best pose prepared by Smina for each complex in the DUD-E benchmark. Each label on x-axis means the data augmentation strategies used for training PIGNet2. For example, NDA (O) means the model trained with NDA and PDA (X) means the model trained without PDA. The red bar shows PIGNet2 model with the best performance. (C) Ablation study about data augmentation strategies for PIGNet2 on predicted distributions of actives and decoys of the DUD-E benchmark. Three models are compared: the model trained without any data augmentation strategies (left), the model trained with NDA alone (middle), and the model trained with both NDA and PDA (right). In each sub-figure, the green colored region is an overlap between the distributions of actives and decoys.

GenScore. Likewise, PIGNet2 showed superior or competitive performance in the DUD-E benchmark, except for EF_{0.5%}.

3.2.4 Ablation study on data augmentation strategies. To elucidate the impact of our data augmentation strategies on the screening performance, we conducted ablation studies based on EF_{1%} results of models trained with and without NDA and PDA in the DUD-E benchmark as shown in Fig. 2(B). It is noteworthy that

we employed the same dataset to compare the EF_{1%} of PIGNet2 with OnionNet-SFCT (Vina), which used only the best structure for each ligand generated by Smina for all ablation studies since the provided data from GenScore does not fully contain all of the original data in the DUD-E benchmark.

First, we observed that a model solely trained on crystal structures without both PDA and NDA exhibited no increase in

Table 3 Results of the DEKOIS2.0 and DUD-E benchmarks. EF_{0.5%}, EF_{1.0%}, and EF_{5.0%} are top 0.5%, 1.0%, and 5.0% enrichment factor, respectively. All metrics were computed by averaging values for all targets. The AUROC and BEDROC metrics were calculated with RDKit.⁶⁴ For PIGNet2, we report the results of the ensemble of 4 randomly initialized models trained with both positive and negative data augmentation. The results of the other models were taken from Hou *et al.*³⁸ The best performance is shown in bold, while the second-best is shown in the italics

Model	DEKOIS2.0				DUD-E					
	AUROC	BEDROC ($\alpha = 80.5$)	EF _{0.5%}	EF _{1.0%}	EF _{5.0%}	AUROC	BEDROC ($\alpha = 80.5$)	EF _{0.5%}	EF _{1.0%}	EF _{5.0%}
Glide SP	0.747	0.385	14.6	12.5	6.30	0.820	0.414	29.44	23.61	9.24
GenScore (GT_ft_0.5)	0.757	<i>0.539</i>	20.2	<i>17.9</i>	8.25	<i>0.824</i>	0.534	41.1	<i>33.3</i>	<i>10.7</i>
GenScore(GatedGCN_ft_1.0)	0.753	0.503	18.6	17.0	7.93	<i>0.824</i>	0.515	<i>38.9</i>	<i>31.2</i>	<i>10.6</i>
PIGNet2	0.812	0.544	20.0	18.6	9.71	0.850	<i>0.515</i>	<i>36.8</i>	<i>31.2</i>	11.2



EF_{1%} after incorporating PDA. This result was expected since PDA helps the model predict affinities for near-native conformations of true binders rather than discriminating diverse decoys as NDA does. However, adding PDA to a model already improved by NDA (NDA-only model) further improved its performance compared to a model trained with NDA alone. The fact that the gain in EF_{1%} by PDA is more prominent in the NDA-only model than in the model without both PDA and NDA indicates that PDA helps better discriminate active and decoy structures that are indistinguishable by the NDA-only model. This suggests that PDA can effectively regularize undesirable biases caused by NDA. In the comparison of the EF_{1%} between the model with and without the data augmentation, the former performed three times better than the latter.

Next, we plotted the distribution of predicted binding affinities for the DUD-E benchmark, as shown in Fig. 2(C), to analyze how the use of each data augmentation leads to an improvement in EF_{1%}. The model without data augmentation is on the left, the one with only NDA is in the middle, and the one with both NDA and PDA is on the right. Without the data augmentation, the two distributions have only a small deviation, indicating the discrimination between actives and decoys is difficult, resulting in a low value of EF_{1%}. However, the deviation increased as more data augmentation strategies were applied, leading to the notable enhancement of EF_{1%}.

Interestingly, applying NDA to the model induced a shift of both distributions to the right. This could be associated with the hinge loss used for NDA, and degraded both the screening and scoring performance. When PDA was added to the model trained with NDA, the distribution of actives shifted less than that of decoys, and hence the two distributions are more separated, particularly at high binding affinity regions. This result directly accounts for the increase in EF_{1%}, as EF_{1%} measures the proportion of active molecules in the top 1% of predictions.

To additionally support the analysis above, we evaluated how much the two distributions are separated in terms of D_{KL} . A greater D_{KL} is obviously associated with a high EF_{1%} value since a greater D_{KL} means a larger separation of the two distributions. As depicted in Fig. 2(C), the D_{KL} of the model with no data augmentation, the NDA-only model, and the model with both

NDA and PDA are 0.235, 0.923, and 1.22, respectively, manifesting the positive effects of NDA and PDA.

3.3 Performance on ranking structurally similar compounds

Selecting molecules with higher binding affinities to a target among plenty of similar derivatives is important during hit-to-lead and lead optimization. For this purpose, one needs to properly rank the relative binding affinities of similar molecules. However, this remains challenging due to issues such as activity cliffs, where small changes in a molecule can result in significant changes in activity.^{74,75} To further demonstrate the versatility of PIGNet2, we conducted a comparative analysis on derivative benchmarks.

3.3.1 Derivative benchmark. We considered two sets of derivative benchmarks reported in 2015 (ref. 47) and 2020,⁴⁸ respectively. The derivative benchmark 2015 is composed of 199 derivatives and their corresponding experimental binding energies for eight target systems. Similarly, the derivative benchmark 2020 comprises a total of 264 active ligands for eight targets. We leveraged this data to evaluate the ability to rank the relative binding affinities among similar derivatives for a given target, which is assessed by calculating the Pearson correlation coefficient R between predicted and experimental values.

3.3.2 Baseline models. Wang *et al.*⁴⁷ compared the binding affinity prediction performance of several physics-based methods: free energy perturbation (FEP), molecular mechanics with generalized Born and surface area solvation (MM-GB/SA), and Glide SP. Here, we aimed to evaluate methods with comparable computational costs, excluding FEP due to its high computational cost despite its high accuracy. The results of MM-GB/SA, Smina, and Glide SP were computed from a single snapshot of a given complex structure.

As for deep learning models, we only considered models for which the provided code can be readily applied or for which benchmark results were already available. As a result, we selected Sfcnn,²³ OnionNet-SFCT (Vina),²⁷ and GenScore.³⁸ These models adopted different approaches, as discussed in the CASF-2016 benchmark. In summary, MM-GB/SA, Glide SP, and Smina can be categorized as traditional scoring functions, while GenScore, OnionNet-SFCT (Vina), and Sfcnn are deep learning-based PLI prediction models.

Table 4 Results on the derivative benchmark 2015, where R means Pearson correlation coefficient. The results of the models with the asterisk (*) are from Wang *et al.*,⁴⁷ while the others were calculated in this work. For PIGNet2, we report the results of the ensemble of 4 randomly initialized models trained with both positive data augmentation and negative data augmentation. The best performance is shown in bold, while the second-best is shown in the italics

Model	Performance average R	Systems							
		BACE	CDK2	JNK1	MCL1	p38	PTP1B	Thrombin	TYK2
MM-GB/SA ^{47*}	0.40	-0.40	-0.53	0.65	0.42	0.66	0.67	0.93	0.79
Glide SP ^{47*}	0.29	0.00	-0.56	0.24	0.59	0.14	0.55	0.53	0.79
Smina ⁵⁵	0.25	-0.48	0.10	-0.060	0.24	0.52	0.70	0.72	0.24
OnionNet-SFCT (Vina) ²⁷	0.023	-0.48	-0.68	-0.59	0.29	0.50	0.66	0.71	-0.23
Sfcnn ²³	0.084	-0.24	0.044	-0.65	0.12	0.58	0.58	0.041	0.20
GenScore (GT_ft_0.5) ^{38*}	0.57	0.45	0.63	0.63	0.54	0.61	0.52	0.92	0.25
GenScore (GatedGCN_ft_1.0) ^{38*}	0.57	0.35	0.62	0.71	0.47	0.65	0.65	0.88	0.22
PIGNet2	0.64	0.42	0.77	0.36	0.78	0.60	0.76	0.83	0.61



For the derivative benchmark 2015, the result of OnionNet-SFCT (Vina) was obtained by rescoring the docked structures from Autodock Vina. For both GenScore models (GT_ft_0.5 and GatedGCN_ft_1.0), we used the provided structures as-is. The results of the other models were obtained using the structures minimized by Smina. For the derivative benchmark 2020, the results of MM-GB/SA, Glide SP, and Vina were obtained from the Hou *et al.*³⁸ The provided structures were generated by the flexible ligand alignment tool or glide core-constrained docking using the respective reference structure. We again minimized the given structures using Smina when evaluating PIGNet2.

3.3.3 Performance of PIGNet2. The performances of all models on the derivative benchmark 2015 were presented in Table 4. PIGNet2 outperformed all the other models. Glide SP and Smina showed anti-correlated results for specific systems such as BACE and CDK2. PIGNet2 showed better performance than MM-GB/SA, which is based on molecular dynamics and hence expected to be more accurate than the docking methods. Even for the BACE and CDK2 systems where MM-GB/SA displayed anti-correlated tendencies, PIGNet2 shows a positive correlation.

Since the derivative benchmark requires accurate prediction of the binding affinities for structurally similar derivatives, it is a much more challenging task than scoring and ranking in the CASF-2016 benchmark. OnionNet-SFCT (Vina), developed based on Δ learning focusing on virtual screening, showed anti-correlated results in almost all systems, despite its impressive docking power in the CASF-2016 benchmark. Surprisingly, Sfcnn, designed to score binding affinities accurately, performed only marginally better than OnionNet-SFCT (Vina) and poorer than traditional scoring functions. This unsatisfactory performance may be because Sfcnn, as a 3D CNN-based model, was trained exclusively on crystal structures and thus struggled to score structures optimized by Smina. Both GenScore models showed much better performances with no anti-correlation for all targets, which have a slightly lower average R value (0.57) than PIGNet2 (0.64). Furthermore, the performance of PIGNet2 in the derivative benchmark 2015, especially in terms of average R , is surprisingly close to that of PBCNet⁷⁶ (0.65), a model exclusively designed for predicting the relative binding affinities of two given derivatives.

Considering the encouraging results of PIGNet2 in the derivative benchmark 2015, we expected similar success in the

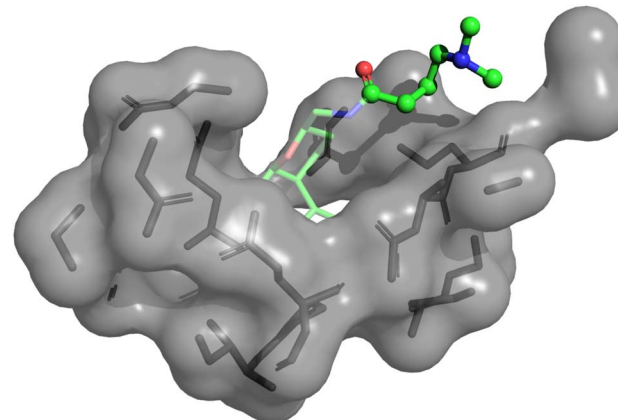


Fig. 3 Illustration of a 3D structure of Eg5-ChEMBL1085692 complex, in which the predicted binding affinity of PIGNet2 is lower than the others, resulting in a negative contribution to the correlation between predicted and experimental binding affinities. In the illustration, the transparent part is the base molecule, while the other part depicted with a ball-and-stick model is an attached flexible chain. The molecular geometries are plotted with PyMol.⁶⁶

derivative benchmark 2020. As shown in Table 5, our model exhibited a remarkable ability compared to traditional physics-based methods. However, the average R value of PIGNet2 (0.43) was slightly lower than the best value of GenScore (0.52) while showing comparable result with the other version of GenScore (0.47). As evaluating eight targets, PIGNet2 showed positive correlations for seven systems, while a negative correlation was observed for the Eg5 system. Interestingly, a more pronounced negative correlation was observed for this particular system in other physics-based methods, suggesting that physics-based approaches may have a peculiar difficulty for this system.

We performed further analysis on why the anti-correlation occurred in the Eg5 system for physics-based approaches including PIGNet2. As Fig. 3 illustrates, the flexible chain in the given molecule prefers to head out to the water rather than fit into the protein pocket. It is expected that the model may less accurately predict the binding affinity of molecules that are more exposed to water, as observed in Eg5, since PIGNet2 like the other physics-based methods considers solvation effects only implicitly. Therefore, PIGNet2 predicted relatively lower binding affinities to molecules with flexible chains. This

Table 5 Results on the derivative benchmark 2020, where R means Pearson correlation coefficient. Except for PIGNet2, all the results are originated from Hou *et al.*³⁸ For PIGNet2, we report the results of the ensemble of 4 randomly initialized models trained with both positive data augmentation and negative data augmentation. The best performance is shown in bold, while the second-best is shown in the italics

Model	Performance average R	Systems							
		HIF2 α	PFKFB3	Eg5	CDK8	SHP2	SYK	c-Met	TNKS2
MM-GB/SA ³⁸	0.35	0.28	0.55	-0.002	0.65	0.59	0.11	0.50	0.16
Glide SP ³⁸	0.30	0.45	0.48	-0.11	0.35	0.54	-0.006	0.38	0.32
Vina ³⁸	0.34	0.49	0.55	-0.52	0.85	0.57	0.52	-0.26	0.54
GenScore (GT_ft_0.5) ³⁸	0.47	0.36	0.45	0.21	0.67	0.61	0.23	0.69	0.54
GenScore (GatedGCN_ft_1.0) ³⁸	0.52	0.52	0.58	0.21	0.71	0.61	0.21	0.73	0.59
PIGNet2	0.43	0.45	0.29	-0.09	0.37	0.72	0.50	0.57	0.64



Table 6 Ablation studies for PIGNet2 on the derivative benchmark 2015, where R means Pearson correlation coefficient. For each model, we report the results of the ensemble of 4 randomly initialized models. The best performance is shown in bold

Model	Data augmentation		Performance average R	Systems							
	Negative	Positive		BACE	CDK2	JNK1	MCL1	p38	PTP1B	Thrombin	TYK2
PIGNet2	X	X	0.50	-0.16	0.36	0.21	0.71	0.67	0.64	0.82	0.74
PIGNet2	X	O	0.54	0.23	0.61	0.33	0.69	0.64	0.76	0.66	0.37
PIGNet2	O	X	0.39	0.085	-0.29	0.25	0.75	0.45	0.32	0.82	0.71
PIGNet2	O	O	0.64	0.42	0.77	0.36	0.78	0.60	0.76	0.83	0.61

analysis highlights the great advantage of physics-based models with high explanatory power, which then provides directions for further improvement.

3.3.4 Ablation study on data augmentation strategies. To understand the impact of PDA on scoring performance, we conducted an ablation study for PIGNet2 on the derivative benchmark 2015. Table 6 shows the influence of NDA and PDA on the scoring performance of PIGNet2 across multiple datasets. Adding NDA to the model caused a slight decrease in the average R . Notably, we observed an inversion of the correlation for CDK2 when NDA was applied, meaning that NDA can negatively affect the scoring performance. When PDA was added, the model regained a high correlation for CDK2. Moreover, the model with PDA alone outperformed the model with no data augmentation in terms of scoring performance. These results suggest an impact of PDA in mitigating potential biases that could occur when training with only crystal structures and NDA alone, thereby improving the scoring performance of PIGNet2.

Incorporating PDA results in maintaining or positively affecting most systems except TYK2. In this context, we have visualized the affinity prediction results for CDK2, the target where applying PDA led to the most significant performance improvement, in Fig. 4. In particular, the figure highlights

a drastic change in the correlation trend from -0.29 to 0.77. This change clearly illustrates the importance of PDA in improving the scoring performance of deep learning models and in overcoming the negative effect of NDA. Consequently, using both PDA and NDA improved the scoring performance of PIGNet2 in the derivative benchmark 2015 from 0.50 to 0.64. This result implies that our data augmentation strategy undoubtedly contributed to the versatility of PIGNet2.

4 Conclusions

In this study, we present PIGNet2, a versatile deep learning-based protein–ligand interaction (PLI) prediction model that enhances its generalization ability with appropriate physics-based inductive bias and a novel data augmentation strategy called positive data augmentation (PDA) in addition to negative data augmentation (NDA). Unlike NDA, PDA generates near-native structures treated as equivalent to crystal structures during training. PIGNet2 incorporates both NDA and PDA, enabling accurate binding affinity prediction for near-native structures and effective discrimination between active and decoy molecules. Remarkably, PIGNet2 outperformed task-specific deep learning models and traditional physics-based methods in all benchmarks and is on par with the state-of-the-art performance reported recently. Furthermore, it has the distinctive advantage of predicting exact binding affinities using intuitively explainable physics, allowing for direct comparison to experimental results and providing directions for further improvement. This result solidifies the potential of PIGNet2 as a versatile deep learning-based PLI prediction model suitable for both scoring and screening tasks in drug discovery.

Despite its high potential, the present method has room for further improvement. First, our generation procedure of binding structures for data augmentation would be biased toward the scoring function of the Smina docking software. This bias results in challenges when dealing with structures generated by other methods. Second, the use of NDA with the hinge loss could lead to lower predicted binding affinities for actives, as observed in the DUD-E benchmark ablation study. Third, better solvation effects should be considered to improve the prediction accuracy for molecules that are more exposed to water as observed in the benchmark result of the eg5 system. Fourth, exploring better physics terms for energy evaluation is expected to enhance the performance significantly, as the present physics terms adopted from conventional docking methods impose strong constraints in the training process and

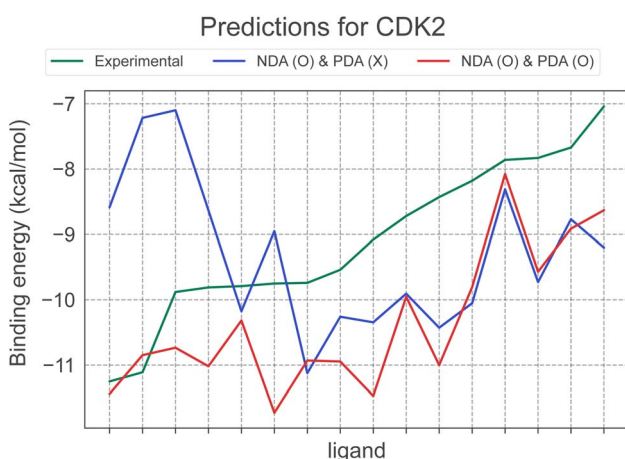


Fig. 4 A case study for a CDK2 target system for ablation study about PDA on the derivative benchmark. The CDK2 system has 16 derivatives in total, and the illustrated result is sorted based on the experimental binding energy for all derivatives. Specifically, this figure additionally illustrates the prediction results of two models: the model trained with NDA alone and the model trained with both NDA and PDA.



thus limit the power of deep learning. Future studies may address these issues to enhance the reliability of PLI prediction models in the drug discovery process.

Data availability

The code and trained models are available at github: <https://github.com/ACE-KAIST/PIGNet2>. Also, data is available at <https://doi.org/10.5281/zenodo.8091220>.

Author contributions

Conceptualization: S. M. and W. Y. K.; methodology: S. M. and J. L.; software, investigation, and formal analysis: S. M., S.-Y. H.; writing – original draft S. M.; writing – review & editing: S. M., S.-Y. H., J. L., and W. Y. K.; supervision: W. Y. K.

Conflicts of interest

There are no conflicts to declare.

Acknowledgements

This work was supported by the National Research Foundation of Korea (NRF) grant funded by the Korea government (MSIT) (RS-2023-00257479).

References

- O. Guvench and A. D. MacKerell, *Curr. Opin. Struct. Biol.*, 2009, **19**, 56–61.
- A. Masoudi-Nejad, Z. Mousavian and J. H. Bozorgmehr, *In Silico Pharmacol.*, 2013, **1**, 17.
- N. Hansen and W. F. van Gunsteren, *J. Chem. Theory Comput.*, 2014, **10**, 2632–2647.
- B. K. Shoichet, S. L. McGovern, B. Wei and J. J. Irwin, *Curr. Opin. Chem. Biol.*, 2002, **6**, 439–446.
- J. Fan, A. Fu and L. Zhang, *Quant. Biol.*, 2019, **7**, 83–89.
- J. D. Chodera, D. L. Mobley, M. R. Shirts, R. W. Dixon, K. Branson and V. S. Pande, *Curr. Opin. Struct. Biol.*, 2011, **21**, 150–160.
- I. Muegge and Y. Hu, *ACS Med. Chem. Lett.*, 2023, **14**, 244–250.
- S.-Y. Huang, S. Z. Grinter and X. Zou, *Phys. Chem. Chem. Phys.*, 2010, **12**, 12899–12908.
- H. Li, K.-H. Sze, G. Lu and P. J. Ballester, *Wiley Interdiscip. Rev. Comput. Mol. Sci.*, 2020, **11**, e1478.
- P. J. Ballester and J. B. O. Mitchell, *Bioinformatics*, 2010, **26**, 1169–1175.
- D. Zilian and C. A. Sottriffer, *J. Chem. Inf. Model.*, 2013, **53**, 1923–1933.
- G.-B. Li, L.-L. Yang, W.-J. Wang, L.-L. Li and S.-Y. Yang, *J. Chem. Inf. Model.*, 2013, **53**, 592–600.
- H. Öztürk, A. Özgür and E. Ozkirimli, *Bioinformatics*, 2018, **34**, 821–829.
- I. Lee, J. Keum and H. Nam, *PLoS Comput. Biol.*, 2019, **15**, 1–21.
- J. Jiménez, M. Škalič, G. Martínez-Rosell and G. D. Fabritiis, *J. Chem. Inf. Model.*, 2018, **58**, 287–296.
- Y. Kwon, W.-H. Shin, J. Ko and J. Lee, *Int. J. Mol. Sci.*, 2020, **21**, 8424.
- Z. Zhang, L. Chen, F. Zhong, D. Wang, J. Jiang, S. Zhang, H. Jiang, M. Zheng and X. Li, *Curr. Opin. Struct. Biol.*, 2022, **73**, 102327.
- J. Gabel, J. Desaphy and D. Rognan, *J. Chem. Inf. Model.*, 2014, **54**, 2807–2815.
- C. Shen, Y. Hu, Z. Wang, X. Zhang, J. Pang, G. Wang, H. Zhong, L. Xu, D. Cao and T. Hou, *Brief. Bioinform.*, 2020, **22**, bbaa070.
- J. Yang, C. Shen and N. Huang, *Front. Pharmacol.*, 2020, **11**, 69.
- M. Su, G. Feng, Z. Liu, Y. Li and R. Wang, *J. Chem. Inf. Model.*, 2020, **60**, 1122–1136.
- Z. Wang, L. Zheng, Y. Liu, Y. Qu, Y.-Q. Li, M. Zhao, Y. Mu and W. Li, *Front. Chem.*, 2021, **9**, 753002.
- Y. Wang, Z. Wei and L. Xi, *BMC Bioinf.*, 2022, **23**, 222.
- O. Méndez-Lucio, M. Ahmad, E. A. del Rio-Chanona and J. K. Wegner, *Nat. Mach. Intell.*, 2021, **3**, 1033–1039.
- C. Shen, X. Zhang, Y. Deng, J. Gao, D. Wang, L. Xu, P. Pan, T. Hou and Y. Kang, *J. Med. Chem.*, 2022, **65**, 10691–10706.
- Z. Wang, L. Zheng, S. Wang, M. Lin, Z. Wang, A. W.-K. Kong, Y. Mu, Y. Wei and W. Li, *Brief. Bioinform.*, 2022, **24**, bbac520.
- L. Zheng, J. Meng, K. Jiang, H. Lan, Z. Wang, M. Lin, W. Li, H. Guo, Y. Wei and Y. Mu, *Brief. Bioinform.*, 2022, **23**, bbac051.
- C. Shen, Y. Hu, Z. Wang, X. Zhang, J. Pang, G. Wang, H. Zhong, L. Xu, D. Cao and T. Hou, *Brief. Bioinform.*, 2021, **22**, bbaa070.
- R. Meli, A. Anighoro, M. J. Bodkin, G. M. Morris and P. C. Biggin, *J. Cheminf.*, 2021, **13**, 59.
- A. R. Leach, B. K. Shoichet and C. E. Peishoff, *J. Med. Chem.*, 2006, **49**, 5851–5855.
- K. Huang, C. Xiao, L. M. Glass and J. Sun, *Bioinformatics*, 2020, **37**, 830–836.
- T. Pahikkala, A. Airola, S. Pietila, S. Shakyawar, A. Szwajda, J. Tang and T. Aittokallio, *Brief. Bioinform.*, 2014, **16**, 325–337.
- M. Volkov, J.-A. Turk, N. Drizard, N. Martin, B. Hoffmann, Y. Gaston-Mathé and D. Rognan, *J. Med. Chem.*, 2022, **65**, 7946–7958.
- S. Moon, W. Zhung, S. Yang, J. Lim and W. Y. Kim, *Chem. Sci.*, 2022, **13**, 3661–3673.
- P. G. Francoeur, T. Masuda, J. Sunseri, A. Jia, R. B. Iovanisci, I. Snyder and D. R. Koes, *J. Chem. Inf. Model.*, 2020, **60**, 4200–4215.
- C. Shen, X. Hu, J. Gao, X. Zhang, H. Zhong, Z. Wang, L. Xu, Y. Kang, D. Cao and T. Hou, *J. Cheminf.*, 2021, **13**, 81.
- H. Li, K.-S. Leung, M.-H. Wong and P. J. Ballester, *BMC Bioinform.*, 2016, **17**, 308.
- T. Hou, C. Shen, X. Zhang, C.-Y. Hsieh, Y. Deng, D. Wang, L. Xu, J. Wu, D. Li, Y. Kang, *et al.*, *Chem. Sci.*, 2023, 8129–8146.
- Z. Cang and G.-W. Wei, *PLoS Comput. Biol.*, 2017, **13**, e1005690.



40 D. D. Nguyen and G.-W. Wei, *J. Chem. Inf. Model.*, 2019, **59**, 3291–3304.

41 C. Yang and Y. Zhang, *J. Chem. Inf. Model.*, 2022, **62**, 2696–2712.

42 Z. Meng and K. Xia, *Sci. Adv.*, 2021, **7**, eabc5329.

43 X. Liu, H. Feng, J. Wu and K. Xia, *PLoS Comput. Biol.*, 2022, **18**, e1009943.

44 M. Su, Q. Yang, Y. Du, G. Feng, Z. Liu, Y. Li and R. Wang, *J. Chem. Inf. Model.*, 2018, **59**, 895–913.

45 M. M. Mysinger, M. Carchia, J. J. Irwin and B. K. Shoichet, *J. Med. Chem.*, 2012, **55**, 6582–6594.

46 M. R. Bauer, T. M. Ibrahim, S. M. Vogel and F. M. Boeckler, *J. Chem. Inf. Model.*, 2013, **53**, 1447–1462.

47 L. Wang, Y. Wu, Y. Deng, B. Kim, L. Pierce, G. Krilov, D. Lupyán, S. Robinson, M. K. Dahlgren, J. Greenwood, D. L. Romero, C. Masse, J. L. Knight, T. Steinbrecher, T. Beuming, W. Damm, E. Harder, W. Sherman, M. Brewer, R. Wester, M. Murcko, L. Frye, R. Farid, T. Lin, D. L. Mobley, W. L. Jorgensen, B. J. Berne, R. A. Friesner and R. Abel, *J. Am. Chem. Soc.*, 2015, **137**, 2695–2703.

48 C. E. Schindler, H. Baumann, A. Blum, D. Böse, H.-P. Buchstaller, L. Burgdorf, D. Cappel, E. Chekler, P. Czodrowski, D. Dorsch, *et al.*, *J. Chem. Inf. Model.*, 2020, **60**, 5457–5474.

49 Z. Liu, M. Su, L. Han, J. Liu, Q. Yang, Y. Li and R. Wang, *Acc. Chem. Res.*, 2017, **50**, 302–309.

50 H. M. Berman, *Nucleic Acids Res.*, 2000, **28**, 235–242.

51 H. Li, K.-S. Leung, M.-H. Wong and P. J. Ballester, *Molecules*, 2015, **20**, 10947–10962.

52 S. Wang, J. Witek, G. A. Landrum and S. Riniker, *J. Chem. Inf. Model.*, 2020, **60**, 2044–2058.

53 A. K. Rappé, C. J. Casewit, K. Colwell, W. A. Goddard III and W. M. Skiff, *J. Am. Chem. Soc.*, 1992, **114**, 10024–10035.

54 T. A. Halgren, *J. Comput. Chem.*, 1996, **17**, 490–519.

55 D. R. Koes, M. P. Baumgartner and C. J. Camacho, *J. Chem. Inf. Model.*, 2013, **53**, 1893–1904.

56 O. Trott and A. J. Olson, *J. Comput. Chem.*, 2010, **31**, 455–461.

57 A. Cereto-Massagué, L. Guasch, C. Valls, M. Mulero, G. Pujadas and S. Garcia-Vallvé, *Bioinformatics*, 2012, **28**, 1661–1662.

58 W. Li and A. Godzik, *Bioinformatics*, 2006, **22**, 1658–1659.

59 L. Fu, B. Niu, Z. Zhu, S. Wu and W. Li, *Bioinformatics*, 2012, **28**, 3150–3152.

60 InterBioScreen Ltd, <http://www.ibscreen.com>.

61 E. W. Bell and Y. Zhang, *J. Cheminf.*, 2019, **11**, 1–9.

62 J. Word, S. C. Lovell, J. S. Richardson and D. C. Richardson, *J. Mol. Biol.*, 1999, **285**, 1735–1747.

63 P. J. Ropp, J. C. Kaminsky, S. Yablonski and J. D. Durrant, *J. Cheminf.*, 2019, **11**, 1–8.

64 RDKit: Open-source cheminformatics, <http://www.rdkit.org>.

65 N. M. O'Boyle, M. Banck, C. A. James, C. Morley, T. Vandermeersch and G. R. Hutchison, *J. Cheminf.*, 2011, **3**, 1–14.

66 L. L. C. Schrödinger, *The PyMOL Molecular Graphics System*, Version 1.8 Schrödinger, LLC., 2015.

67 C. M. Bishop, *Mixture density networks*, Aston University, 1994.

68 L. Chen, A. Cruz, S. Ramsey, C. J. Dickson, J. S. Duca, V. Hornak, D. R. Koes and T. Kurtzman, *PLoS One*, 2019, **14**, e0220113.

69 N. Triballeau, F. Acher, I. Brabet, J.-P. Pin and H.-O. Bertrand, *J. Med. Chem.*, 2005, **48**, 2534–2547.

70 J.-F. Truchon and C. I. Bayly, *J. Chem. Inf. Model.*, 2007, **47**, 488–508.

71 S. Kullback and R. A. Leibler, *Ann. Math. Stat.*, 1951, **22**, 79–86.

72 J. Sunseri and D. R. Koes, *Molecules*, 2021, **26**, 7369.

73 R. A. Friesner, J. L. Banks, R. B. Murphy, T. A. Halgren, J. J. Klicic, D. T. Mainz, M. P. Repasky, E. H. Knoll, M. Shelley, J. K. Perry, D. E. Shaw, P. Francis and P. S. Shenkin, *J. Med. Chem.*, 2004, **47**, 1739–1749.

74 G. M. Maggiore, *J. Chem. Inf. Model.*, 2006, **46**, 1535.

75 D. van Tilborg, A. Alenicheva and F. Grisoni, *J. Chem. Inf. Model.*, 2022, **62**, 5938–5951.

76 J. Yu, Z. Li, G. Chen, X. Kong, J. Hu, D. Wang, D. Cao, Y. Li, X. Liu, G. Wang, *et al.*, *ChemRxiv*, 2023, preprint, DOI: [10.26434/chemrxiv-2023-tbmtt](https://doi.org/10.26434/chemrxiv-2023-tbmtt).

